JOURNAL OF COMPUTATIONAL PHYSICS 72, 220–242 (1987)

"Hybrid" Monte Carlo Simulation of Ripple Transport in Stellarators

C. D. BEIDLER, W. N. G. HITCHON, AND J. L. SHOHET

Torsatron/Stellarator Laboratory, University of Wisconsin-Madison, 1415 Johnson Drive, Madison, Wisconsin 53706

Received September 17, 1986; revised December 24, 1986

A rapid "hybrid" Monte Carlo simulation has been developed to investigate helical ripple transport at low collision frequencies in stellarators. The simulation is a hybrid in the sense that the majority of ripple trapped particles are followed through the iterative conservation of their longitudinal adiabatic invariant, J, while those particles in a narrow region of phase space on either side of the ripple trap/detrap boundary are followed using guiding center equations of motion. This formulation is much faster than a purely guiding center treatment, making all collision frequency regimes of interest accessible at reasonable costs in computer time. It is shown that local toroidal variation of the magnetic field yields considerably more complicated trapping/detrapping orbits than allowed in analytic theory and that the form of J used in this work correctly describes this behavior. The methods employed allow the examination of stellarator configurations for which the magnitude of the toroidal well, ε_t, is larger than that of the helical well, ε_h, as well as configurations more often treated in which $\varepsilon_h > \varepsilon_t$. Results are obtained for the usual analytic model of the helical ripple, $\varepsilon_h = \varepsilon_h(r)$, as well as a more realistic model for which $\varepsilon_h = \varepsilon_h(r, \theta)$. It is shown that even a rather weak dependence of ε_h on poloidal angle can alter the magnitude of the diffusion coefficient as well as its scaling with collision frequency.

INTRODUCTION

The success of stellarator experiments in recent years has prompted renewed interest in the device as a viable candidate for a fusion reactor. Much of this interest has centered on the transport properties of the stellarator at the low collision frequencies expected to be typical in such reactors, primarily since the inhomogeneity in the stellarator's magnetic field introduces a significant loss mechanism over and above those predicted by neoclassical theory in an axisymmetric tokamak. Analytic theories [1–5] have attempted to examine the collisionality regimes in question, but are usually forced to make simplifying assumptions in order to make the problem tractable. Guiding center Monte Carlo computer codes [6–11] have been employed to examine the problem, but the long run times required at low collision frequencies make this a costly and time consuming solution.

Recently, numerical simulations have appeared which make use of "averaged" equations to describe more rapidly the behavior of trapped particles [12–14]. These

0021-9991/87 $3.00

computational methods are efficient enough to examine collision frequencies of interest, but each either simplifies, or ignores altogether, potentially significant physical effects. Many of these simplifications make it impossible to correctly describe the important processes associated with particles trapping and detrapping in local helical wells. In order to treat these physical effects one must ensure that the drift velocity is correct near the ripple trap/detrap boundary, enabling an accurate calculation of the trapping probability. A related point is that nonzero rotational transform per field period introduces local toroidal variation of the magnetic field within a single ripple period, invalidating the analytic assumptions as to ripple geometry. This alters the variation of a localized particle's depth in a helical well as it undergoes its drift motion, changing its detrapping point and potentially providing a wider variety of particle orbits than treated by analytic theory. Finally, one must allow for the inherently nonadiabatic nature of the trapping/detrapping process which dictates that the conservation of the longitudinal adiabatic invariant cannot be assumed.

One way to properly treat the complicated processes at this boundary numerically is to use the more detailed level of description provided by guiding center equations of motion. In order to preserve the speed of the simulation it is desirable to limit the use of the guiding center equations to as small a region of phase space as possible, using the techniques of an earlier bounce-averaged code [12] whenever possible. The result, a "hybrid" bounce-averaged guiding center Monte Carlo simulation, correctly describes the behavior of ripple trapped particles in a fraction of the time necessary to follow such particles entirely with guiding center equations. Using this approach we have been able to examine transport at low collision frequency including all the physical effects listed above for the first time.

This paper is organized as follows. In Section I, we introduce analytic forms for the magnitudes of the magnetic field and helical ripple. In Section II, we introduce the quantity k^2, which indicates the trapping state of a particle, as well as J, the longitudinal adiabatic invariant. Employing forms of these two quantities which avoid the usual analytic assumptions, we show that the trapping/detrapping behavior is much more complicated than assumed in analytic theory. In Section III, the "hybrid" numerical simulation which employs these "improved" forms of J and k^2, along with guiding center equations near the ripple trap/detrap boundary is described. The difficulties of matching these two at their interface are also described. Results and discussion are provided in Section IV and Section V contains concluding remarks.

I. The Model Field

In order to begin our discussion of particle orbits and the resulting transport we introduce the model field and the accompanying notation. We assume the usual analytic form for the magnitude of the stellarator field

$$B = B_0(1 + \varepsilon_t(r)\cos\theta - \varepsilon_h(r,\theta)\cos(l\theta + p\phi)). \tag{1}$$

In this paper r is the minor radial variable and labels a flux surface, θ is the poloidal angle, ϕ is the toroidal angle, B_0 is the field on axis, l is the multipolarity of the device, p is the number of field periods, $\varepsilon_t = r/R_0$ where R_0 is the major radius of the torus, and ε_h is the magnitude of the helical ripple. In most analytic work it is assumed that ε_h is independent of poloidal angle and given by

$$\varepsilon_h = \varepsilon \rho^l \delta_0 h \tag{2}$$

where $\varepsilon \equiv \varepsilon_t(a) = a/R_0$ is the inverse aspect ratio at the plasma edge, $\rho = r/a$, δ_0 is a constant, and $h \equiv \varepsilon p^2/l$. However, it has been shown [15] that this form of the helical ripple is only valid when $h \gg 1$ and that for the more general case

$$\varepsilon_h = \varepsilon \rho^{(l-1)} \delta_0 h (z_0^2 + \rho^2 - 2 z_0 \rho \cos\theta)^{1/2}, \tag{3}$$

where $z_0 = h^{-1}$. It is easily seen that as $z_0 \to 0$ the expression in (2) is recovered. Since h is seldom very large in actual devices the more general form of ε_h can often differ substantially from that given in (2). A comparison of magnetic field strengths obtained using the two forms of ε_h may be found in Figs. 1–2 for values of $h = 7.2$ (configuration 1—Fig. 1) and $h = 0.9$ (configuration 2—Fig. 2). From these it is clear that for small h, Eq. (2) is quite an unrealistic approximation to the helical ripple amplitude, significantly underestimating the magnitude of ε_h over much of the poloidal cross section.

In what follows, when we speak of "the θ-dependent" ripple profile we are referring to the ε_h of (3); when the terms "traditional" and "standard" are used it will be in the context of describing the helical ripple of (2).

TABLE I

Parameter	Configuration 1	Configuration 2
Field on axis (B_0)	4 T	4 T
Major radius (R_0)	20 m	10 m
Minor radius (a)	2 m	2 m
Multipolarity (l)	2	2
Field periods (p)	12	3
Ripple constant (δ_0)	0.35	0.40
$\langle \varepsilon_h \rangle$ at launch		
Traditional ripple	0.063	0.018
θ-Dependent ripple	0.065	0.043
Rotational transform (ι)	1.47	0.48
Launch radius (r_0)	1 m	1 m
Electrostatic potential	$\pm 15{,}000(1-(r/a)^2)$ V	$-15{,}000(1-(r/a)^2)$ V
Proton plasma		
Test particle energy	12 KeV	6 KeV
Background energy	10 KeV	6 KeV

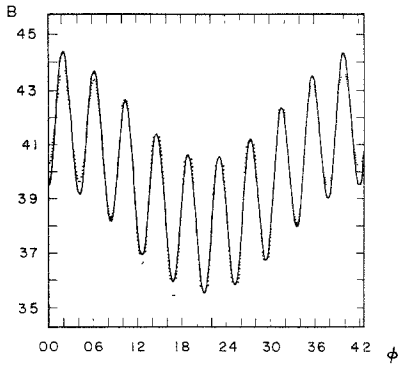

FIG. 1. The magnitude of B along a field line is plotted versus toroidal angle using the "standard" form of the helical ripple given by (2) (solid line), and the more realistic θ-dependent ripple profile of (3) (broken line), for the parameters of configuration 1.

II. Describing Particle Orbits

The stellarator field of (1) is characterized by local magnetic wells along a field line. Particles become entrapped in these local wells and thus have an opportunity to drift unidirectionally for a significant length of time. At the collision frequencies of interest, ions and electrons have unequal diffusion rates, giving rise to an ambipolar electric field. The presence of the electric field (assumed to be radial, that is, in the flux coordinate representation, to have no component along B) leads to a poloidal $E \times B$ drift with frequency $\Omega_E = E_r/rB$, limiting the radial excursion of ripple trapped particles off a flux surface to $\Delta r \approx v_d/\Omega_E$, where v_d is the ∇B drift velocity. At low collision frequencies it is expected that this behavior will give rise to the dominant transport mechanism.

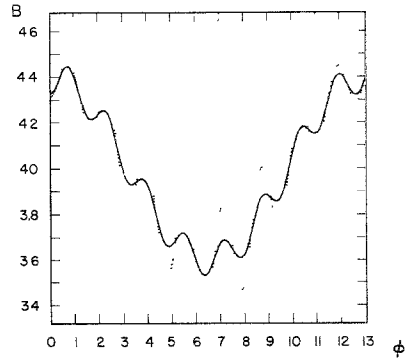

FIG. 2. As in Fig. 1 for the parameters of configuration 2.

To aid in the description of ripple transport the quantity k^2, which indicates the trapping state, is introduced,

$$k^2 = \frac{\kappa/\mu - B_n}{B_x - B_n}, \tag{4}$$

where $\kappa = mv^2/2$, $\mu = mv_\perp^2/2B$, and $B_n(B_x)$ is the local minimum (maximum) value of the magnetic field. Ripple-trapped particles have values of k^2 between 0 and 1, corresponding respectively to those particles trapped at the bottom of a helical well and those which are marginally trapped.

Analytic theories which attempt to describe the behavior of ripple-trapped particles make extensive use of the bounce action, J,

$$J = \frac{1}{2\pi} \oint m v_\parallel \, dl \tag{5}$$

which is a constant of the collisionless motion and where

$$v_\parallel = \left\{ \frac{2}{m} (\kappa - \mu B) \right\}^{1/2}. \tag{6}$$

It is usually assumed in analytic theory that $\varepsilon_h > \varepsilon_t$ and the rotational transform per field period is small so that the local toroidal variation of the magnetic field may be ignored. Then the bounce action may be written

$$J = \frac{2R}{(l\iota + p)} (\mu B_0 m \varepsilon_h)^{1/2} \frac{1}{2\pi} \oint (k^2 - \sin^2(\eta/2))^{1/2} \, d\eta, \tag{7}$$

where ι is the rotational transform, $R = R_0 - r\cos\theta$, $\eta = l\theta + p\phi$ and where k^2 takes the form

$$k^2 = \frac{\kappa/\mu B_0 - 1 - \varepsilon_t \cos\theta + \varepsilon_h}{2\varepsilon_h}. \tag{8}$$

The assumption that the local toroidal variation of B is ignorable has been used here to obtain $B_n(B_x)$ by setting $\eta = 0$ $(\eta = \pi)$ in (1) and substituting into (4). Under this assumption, the local well is symmetric with adjacent maxima being of equal height. With these stipulations

$$A(k^2) = \frac{1}{2\pi} \oint (k^2 - \sin^2(\eta/2))^{1/2} \, d\eta = \frac{4}{\pi} \{ E(k) - (1 - k^2) K(k) \}, \tag{9}$$

where K and E are the complete elliptic integrals of the first and second kind, respectively.

In any real device, however, the local toroidal variation of B is not zero, the well is not symmetric, and (8) yields a $k^2 = 1$ curve like that shown in Fig. 3a (for con-

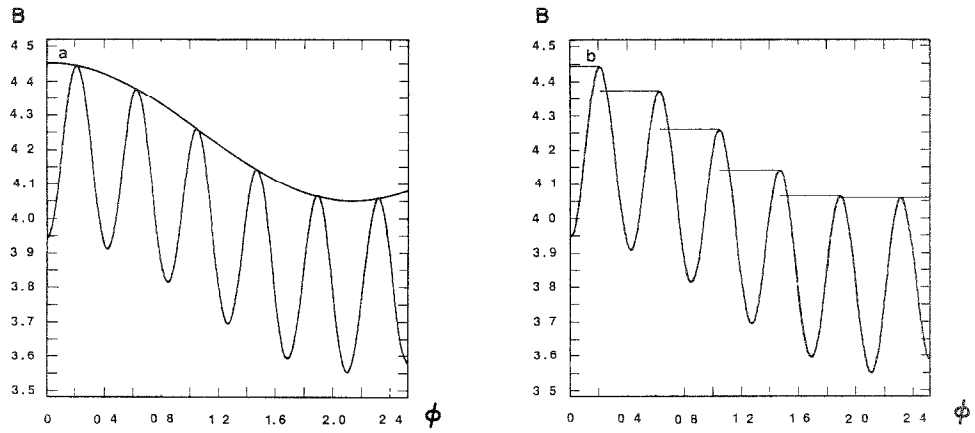

FIG. 3. (a) The $k^2 = 1$ curve obtained from (8) is shown relative to the model field of (1) for the parameters of configuration 1. Note that particles with values of k^2 less than 1 need not be ripple trapped. (b) An alternate definition of the $k^2 = 1$ curve obtained from (4) by setting B_n equal to the local minimum value of B and B_ν equal to the lower of the two local maxima of B. This form of k^2 has discontinuous jumps as a particle travels over one ripple well to the next. However, all particles with $k^2 < 1$ are ripple trapped.

figuration 1). If we define k^2 by (8), we see that it becomes possible for a particle which is not ripple trapped (in the sense we usually think of a localized particle) to have $k^2 < 1$. As the ratio $\varepsilon_h/\varepsilon_t$ becomes smaller, or ι/p becomes significant, toroidal effects become steadily more important and the $k^2 = 1$ curve defined by (8) becomes less and less representative of the true trap/detrap boundary.

Clearly, if k^2 is to be used as an index to determine if a particle is ripple trapped (and if so, how deeply) effects of the local toroidal variation of B must be included by constructing a "localized" form, as shown in Fig. 3b. That is, as a particle travels over one ripple well to the next, its value of k^2 changes discontinuously. Returning to (4), we see that such a formulation for k^2 is possible if we choose

(1) $B_n = B_{\min}$, the local minimum value of B

(2) $B_\nu = B_{\max}$, the lower of the two local maxima of B.

In order to continue using an equation for the bounce action which is of the form of (7) (containing complete elliptic integrals), it is necessary to construct a symmetric "effective" well. This is similar to what is often done in the study of rippled tokamaks [16, 5] although the constraints applied here are somewhat different. The "effective" magnetic field, $\bar{B}$, is uniquely defined by meeting three stipulations:

(1) $\bar{B}_{\min} = B_{\min}$

(2) $\bar{B}_{\max} = B_{\max}$, the lower of the two local maxima of B

(3) $\bar{B} = B$ at the two local values of ϕ, denoted ϕ_1 and ϕ_2, where $k^2 = k^2_{BA}$, i.e.,

$$B = \bar{B} = B_{\min} + k^2_{BA}(B_{\max} - B_{\min}),$$

where k_{BA}^2 is an (as of yet) arbitrary value of k^2 satisfying $0 < k_{BA}^2 < 1$. (It will subsequently become clear in the next section that this final restriction was chosen so that the actual and effective wells have identical values of B at the transition value of k^2 where the numerical simulation changes from using a bounce-averaged formalism to guiding center equations). We then obtain

$$\bar{B} = \frac{B_{max} + B_{min}}{2} \left\{ 1 - \frac{B_{max} - B_{min}}{B_{max} + B_{min}} \cos \bar{\eta} \right\}, \tag{10}$$

where

$$\bar{\eta} = \frac{(\phi_1 + \phi_2 - 2\phi)(\pi/2 - \sin^{-1}(1 - 2k_{BA}^2))}{(\phi_1 - \phi_2)}. \tag{11}$$

Using the effective well, it is possible to express the bounce action

$$J = \frac{2R(\phi_2 - \phi_1)}{\pi - 2\sin^{-1}(1 - 2k_{BA}^2)} \left\{ \frac{\mu m (B_{max} - B_{min})}{2} \right\}^{1/2} A(k^2), \tag{12}$$

where k^2 is now given by

$$k^2 = \frac{\kappa/\mu - B_{min}}{B_{max} - B_{min}}.$$

Variation of k^2 With Poloidal Angle for Ripple-Trapped Particles

In this subsection we discuss the variation in the depth of the helical well that a localized particle "sees" as it transits poloidally, limiting the discussion to ripple profiles of the form of (2) since this is the more simple case and the one most often treated in the literature. It will be shown that the quantity used to characterize the "effective" ripple depth seen by the particle, $\varepsilon_h^* \equiv (B_{max} - B_{min})/2B_0$, is substantially more complicated for any realistic stellarator than the usual assumption that $\varepsilon_h^* = \varepsilon_h$. Perhaps more important from our point of view, the higher level of description also significantly alters the expected variation of k^2 with poloidal angle which a localized particle experiences, yielding a more complex variety of trapping and detrapping orbits than those usually allowed in analytic theory. These effects are illustrated by following trapped particle orbits and it is shown that the form of J given by (12) correctly describes this behavior as well.

To find extrema along a field line described by (1) we substitute $\theta = \theta_0 + \iota\phi$, and solve

$$\frac{dB}{d\phi} = B_0(-\varepsilon_t \iota \sin\theta + \varepsilon_h(l + p)\sin\eta) = 0.$$

Extrema exist if

$$\sin\eta = \frac{\varepsilon_t \iota \sin\theta}{\varepsilon_h(l + p)} \equiv \alpha \sin\theta \equiv \alpha^*.$$

For $\alpha > 1$, ripple wells do not exist over part of the poloidal cross-section. This rarely occurs in stellarators although it is the usual state of affairs in a tokamak when the ripple due to the finite nature of the toroidal field coils is considered. (It is customary when discussing rippled tokamaks to define $\alpha^* = \alpha|\sin\theta|$, but for our purposes the absolute value sign will be dropped.)

Taking the next derivative of B with respect to ϕ, it may be shown that maxima occur at

$$\phi_{\max} = \frac{(2n \pm 1)\,\pi - \sin^{-1}\alpha^* - l\theta_0}{(l+p)} \tag{13}$$

and minima occur at

$$\phi_{\min} = \frac{2n\pi + \sin^{-1}\alpha^* - l\theta_0}{(l+p)}. \tag{14}$$

Under the usual idealized analytic assumptions ($\varepsilon_h \gg \varepsilon_t$, $\iota/p \ll 1$) the α^* corrections are negligible and these expressions simplify to ones obtainable by setting $\eta = l\theta_0 + (l+p)\,\phi$ equal to the appropriate multiple of π.

In what follows we assume that the maximum value of $\iota(l+p)^{-1}\sin^{-1}\alpha^*$ is small enough so that the approximations $\sin(\iota(l+p)^{-1}\sin^{-1}\alpha^*) = \iota(l+p)^{-1}\sin^{-1}\alpha^*$ and $\cos(\iota(l+p)^{-1}\sin^{-1}\alpha^*) = 1$ are valid. Substituting Eqs. (13) and (14) into (1) we solve for ε_h^*,

$$\varepsilon_h^* = \varepsilon_h\left\{(1-\alpha^{*2})^{1/2} + \frac{\varepsilon_t\cos\theta}{2\varepsilon_h}(\cos\gamma - 1) + \frac{\alpha}{2}|\cos\theta|\sin\gamma\sin^{-1}\alpha^* - \frac{\varepsilon_t}{2\varepsilon_h}|\sin\theta|\sin\gamma + \frac{\alpha^*}{2}\sin^{-1}\alpha^*(\cos\gamma + 1)\right\}, \tag{15}$$

where $\gamma = \iota\pi/(l+p)$ is a constant for an $l=2$ stellarator. Under idealized conditions, $\alpha \to 0$ and this expression reduces to the trivial $\varepsilon_h^* = \varepsilon_h$.

As stated earlier, we are probably more interested in the variation of k^2 with θ which a localized particle undergoes, since this supplies direct information concerning the particle's depth in the well. Substituting for $B_{\min}$, k^2 takes the form

$$k^2 = \frac{\kappa/\mu - B_0(1 + \varepsilon_t\cos\theta - \varepsilon_h\,\alpha^*\sin^{-1}\alpha^* - \varepsilon_h(1-\alpha^{*2})^{1/2})}{2B_0\,\varepsilon_h^*} \tag{16}$$

Under idealized conditions this reduces to (8). To find the values of poloidal angle at which a localized particle attains its maximum and minimum values of k^2, one solves $dk^2/d\theta = 0$. However, the resulting expression is sufficiently complicated so that it is only useful in limiting cases.

Instead, to test the validity of this expression, actual particle orbits were followed numerically using the parameters of configuration 1. Figure 4 shows the variation of

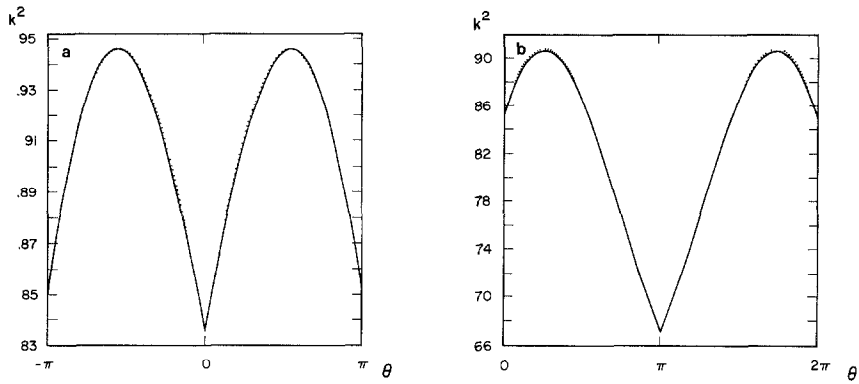

FIG. 4. Variation of k^2 with θ for a particle which remains helically trapped during an entire poloidal transit in the magnetic field of configuration 1. The solid line was obtained by numerically following the particle's orbit while the broken line shows the analytic prediction of equations (15–16). This is done for (a) $E_r > 0$ and (b) $E_r < 0$. Note that figures (a) and (b) are centered about different values of θ.

k^2 with θ obtained by following a particle that remained helically trapped for an entire poloidal transit (solid line) along with the results predicted by (16) (broken line). It should be noted that (16) cannot be plotted without an accurate expression for the variation of r with θ that a ripple-trapped particle experiences as it transits poloidally. In this case we have employed the conservation of the bounce action expressed in (12) to obtain the corresponding value of r at each value of θ. As can be seen from the figure, the combination of (16) and the conservation of J yields excellent agreement with the actual results.

The same exercise is repeated in Fig. 5, where we now consider the idealized case that is most often examined in the literature. This figure was generated by setting $\iota = 0$ but leaving all other machine parameters unchanged. In this limit, the actual k^2 vs θ plot and the analytic expression of (16) coincide. The extrema in k^2 occur at

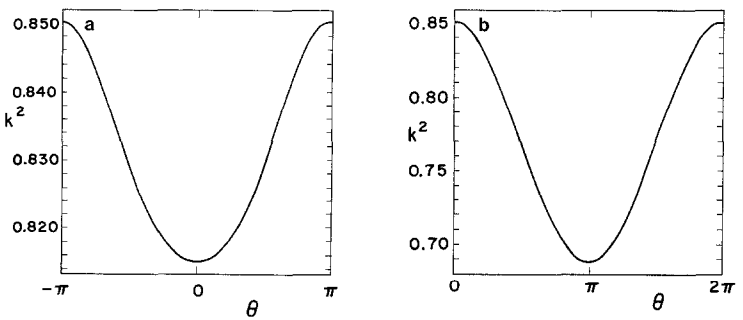

FIG. 5. As in Fig. 4, for the idealized conditions most often treated in the analytic literature, i.e., $\iota = 0$.

the major radial inside and outside of the device. This is not unexpected, since under the assumptions employed,

$$\frac{d\varepsilon_h}{d\theta} = \frac{l\varepsilon_h}{r}\frac{dr}{d\theta} \approx \frac{-l\varepsilon_h}{r}\frac{v_d}{\Omega_E}\sin\theta,$$

where $v_d \equiv \mu/qR$. Thus the extrema in the well depth that a ripple-trapped particle "sees" also occur at the inside and outside of the device. The poloidal drift frequency is in the positive θ direction for $E_r < 0$ and in the negative θ direction for $E_r > 0$. ($\theta = 0$ is taken to be at the inside of the device.) Thus the maximum value of k^2 is obtained at $\theta = 0$ and the minimum at $\theta = \pi$ for $E_r < 0$. The situation is reversed for $E_r > 0$. If we consider the orbits of particles which make transitions from being helically trapped to toroidally blocked (toroidal banana) and back again, we find that each sign of E_r is characterized by one particular type of orbit. For $E_r < 0$ a helically trapped particle detraps as it moves toward the inside of the device ($\theta = 0$). The banana portion of the orbit is, of course, localized toward the outside ($\theta = \pi$) of the device. A projection of this orbit onto a constant theta plane appears crescent shaped. For $E_r > 0$ a helically trapped particle detraps as it moves toward the outside of the device and the banana portion of its orbit continues in this direction. The projection of this orbit appears roughly circular, bulging at one side [12].

However, the variation of k^2, with θ predicted by (16) and verified in Fig. 4, does away with the exclusivity of these orbits. Instead, both types of orbits may exist for either sign of the electric field. That this is indeed the case has been verified by numerically solving and plotting guiding center particle orbits for both signs of E_r.

The development presented here has considered only the simple model of the helical ripple given in (2), in which $\varepsilon_h = \varepsilon_h(r)$. On considering ripple profiles which have a θ dependence as well, such as that of (3) or any of the so-called "transport optimized ripples" [17–19], the situation becomes even more complicated. These cases will not be discussed here but will be examined in greater detail in subsequent work.

III. "Hybrid" Numerical Simulation

In this section we describe a numerical method which iteratively follows the majority of ripple-trapped particles through the iterative conservation of J expressed in (12), while following those particles in a narrow region on either side of the ripple trap/detrap boundary using guiding center equations expressed in flux coordinates.

For the purposes of the hybrid simulation there are three means of describing a particle's orbit, each of which is best classified by the region of k^2 space in which it is used:

(1) Particles for which local collisionless bounce motion has no chance of detrapping the particle have values of k^2 significantly below 1. Bounce-averaging is appropriate for these particles.

(2) As particles approach $k^2 = 1$ from above or below the trap/detrap boundary, more detail is needed to describe their orbits correctly. The accuracy of guiding center equations is required if these particles are to be followed properly.

(3) The remaining particles have significant parallel velocity and are largely unaffected by the local magnetic ripple. These particles are allowed to stream along the field line they currently find themselves on.

For notational convenience the regions may be defined by

(1) Bounce-averaged region—$0 \leqslant k^2 \leqslant k_{BA}^2$

(2) Guiding center region—$k_{GC}^2 \leqslant k^2 \leqslant k_{FS}^2$

(3) Free-streaming region—$k_{FS}^2 < k^2$,

where

$$k_{FS}^2 > 1 > k_{BA}^2 > k_{GC}^2.$$

A particle as it crosses k_{BA}^2 from the bounce-averaged region enters the guiding center region. For the same particle to return to the bounce-averaged region, however, it must cross k_{GC}^2, where $k_{GC}^2 < k_{BA}^2$. The reasons for allowing the bounce-averaged and guiding center regions to overlap will be discussed shortly. Finally, a particle crossing k_{FS}^2 from the guiding center region enters the free-streaming region, and vice-versa.

Trapped particle orbits are followed by advancing the particle's current value of θ and iteratively finding the corresponding value of r which ensures the conservation of J expressed in (12) using a numerical form of Newton's method

$$r_{n+1} = r_n - \frac{(J(r_n) - J_0)(r_n - r_{n-1})}{J(r_n) - J(r_{n-1})}, \tag{17}$$

where J_0 is the value of J to be conserved. Convergence is rapid, typically taking 2–4 iterations.

The time elapsed during the step is calculated by bounce-averaging the drift equation

$$\left\langle \frac{d\theta_0}{dt} \right\rangle = \frac{\mu}{qr}\left(\frac{\cos\theta}{R_0} - \frac{\varepsilon_h l}{r} \langle \cos(l\theta + p\phi) \rangle \right) - \frac{E_r}{B_0 r}, \tag{18}$$

where

$$\langle \cos(l\theta + p\phi) \rangle = \frac{2E(k)}{K(k)} - 1. \tag{19}$$

The elapsed time is then calculated

$$\tau = \frac{(1 + l/p)\, \Delta\theta}{\langle d\theta_0/dt \rangle}. \tag{20}$$

The factor $(1+l/p)$ arises because the step is in θ while the drift equation is expressed in terms of θ_0.

A bounce-averaged equivalent of the Lorentz collision operator is used to scatter a particle's value of k^2, at each time step

$$\Delta k^2 = \frac{\nu\tau}{2\tilde{\varepsilon}_h} \pm \left\{ \left(\frac{2\nu\tau}{\tilde{\varepsilon}_h} \right) \left(\frac{E(k) - (1-k^2)\,K(k)}{K(k)} \right) \right\}^{1/2}, \tag{21}$$

where $\tilde{\varepsilon}_h = (B_{max} - B_{min})/(B_{max} + B_{min})$ and ν is the 90° deflection frequency for ions on ions. The $\pm$ indicates that this term has equal probability of being chosen as positive or negative for any given collision. This numerical expression is valid as long as $(\nu\tau/\tilde{\varepsilon}_h)^{1/2} \ll 1$.

Particle orbits near the trap/detrap boundary are followed by integrating guiding center equations of motion expressed in flux coordinates, [20]. In this simulation the physical space variables are r, θ_0, ϕ, and the drift equations are

$$\begin{aligned} \frac{dr}{dt} &= v_D \left\{ \varepsilon_t \sin\theta - l\varepsilon_h \sin(l\theta + p\phi) + \frac{\partial \varepsilon_h}{\partial \theta_0} \cos(l\theta + p\phi) \right\} \\ \frac{d\theta_0}{dt} &= v_D \left\{ \frac{\cos\theta}{R_0} - \frac{\partial \varepsilon_h}{\partial r} \cos(l\theta + p\phi) \right\} - \frac{E_r}{B_0 r} \\ \frac{d\phi}{dt} &= \frac{v_\parallel}{(R_0 - r\cos\theta)}, \end{aligned} \tag{22}$$

where

$$v_D = \frac{\mu}{qr} + \frac{m v_\parallel^2}{qBr}.$$

Again, a discretized version of the Lorentz collision operator is used after each time step [6]

$$\Delta\lambda = -\nu\lambda\tau \pm \{\nu\tau(1-\lambda^2)\}^{1/2}, \tag{23}$$

where $\lambda = v_\parallel/v$. In the guiding center section, the choice of time step is determined by the corresponding collisional change in k^2 for all but the most collisionless cases. In particular, it was found that $\sqrt{\nu\tau} < 10^{-2}$ is required. This corresponds to a collisional change in k^2 of approximately 0.05. Time steps yielding larger collisional changes were unable to correctly describe the transport processes in this region of phase space for they were incapable of resolving the details of the motion near $k^2 = 1$.

Particles with $k^2 > k_{FS}^2$ are allowed to stream along field lines at a constant radius. Their "equation of motion" is simply that of a field line, $\theta = \theta_0 + \iota\phi$. In a typical stellarator configuration about half of the particle population will lie in this region. In the collisionality regimes of interest it is generally expected that particle

transport due to other than ripple effects is negligible and this is borne out by varying k_{FS}^2 and by comparison of this and other simulations. The rather crude treatment of these particles greatly increases the speed of the simulation. Equation (23) is used to simulate the effect of collisions between particles, but in this section of the code the size of the time step is not so strictly limited as in the guiding center section.

The way in which a particle's orbit is described can change through its drift motion, collisional processes, or simply by passing from the vicinity of one local well to the next (recall that, in general, k^2 changes discontinuously as a particle passes over each local maximum). The transition between the guiding center and free-streaming sections is accomplished with no special problems since all quantities required to describe the particle's orbit are intact and unchanged by the transition.

However, when a particle leaves the bounce-averaged section and enters that in which guiding center equations are used, it is necessary to choose a ripple phase, η, for the particle. To do this, a probability distribution, β, is found which describes the likelihood that the particle will be found at a given value of ripple phase and then randomly choosing from this probability distribution. The differential probability, $d\beta$, may be expressed

$$d\beta = \frac{2(dl/v_\parallel)}{\int dl/v_\parallel} = \frac{d\bar{\eta}/v_\parallel}{2\int_0^{\bar{\eta}_m} d\bar{\eta}/v_\parallel}, \tag{24}$$

where $\bar{\eta}_m$ is the value of $\bar{\eta}$ at which $v_\parallel = 0$. From (12) we obtain

$$v_\parallel = \left\{\frac{2\mu(B_{max} - B_{min})}{m}\right\}^{1/2} \{k^2 - \sin^2 \bar{\eta}/2\}^{1/2}.$$

Substituting,

$$d\beta = \frac{d\bar{\eta}\{k^2 - \sin^2(\bar{\eta}/2)\}^{-1/2}}{2\int_0^{\bar{\eta}_m} d\bar{\eta}\{k^2 - \sin^2(\bar{\eta}/2)\}^{-1/2}}. \tag{25}$$

The integral in the denominator is recognized as the complete elliptic integral of the first kind. Integrating once more to obtain β,

$$\beta = \begin{cases} \frac{1}{2} - F(\psi, k)/2K(k), & -\pi/2 < \psi < 0, \\ \frac{1}{2} + F(\psi, k)/2K(k), & 0 < \psi < \pi/2, \end{cases} \tag{26}$$

where F is the incomplete elliptic integral of the first kind and $\psi = \sin^{-1}(\sin(\bar{\eta}/2)/(k_{BA}^2)^{1/2})$ is a transformation variable.

Depending on the value of ripple phase a particle is assigned as it emerges into the guiding center section, its immediate local drifts may serve to decrease its value of k^2 (pushing it back into the bounce-averaged section), whereas if the particle was followed for an entire helical bounce time, the overall trend in k^2 may or may not be decreasing, depending principally on the poloidal angle. To prevent the particle

being immediately returned to the bounce-averaged region, k^2_{GC}, the value of k^2 at which particles are allowed to enter this region, is set equal to $k^2_{BA} - \delta$, where δ is the largest possible local variation of k^2. The resulting overlap in the regions in which bounce-averaged and guiding center formulations are used is small but sufficient to prevent a particle from being shuttled back and forth rapidly between the two regions. This also ensures that a particle remains in the region for a long enough period of time so that the randomization of $\bar{\eta}$ expressed by (26) is valid.

The Diffusion Coefficient

The calculation of a local diffusion coefficient, D, in a magnetically confined plasma of finite volume can pose several problems. The possibility of unconfined drift orbits in a significant region of velocity space may give rise to convective rather than diffusive behavior. Even if such orbits do not exist, others, in which particles deviate significantly from their original flux surface, while remaining confined, may make the diffusion nonlocal. In both of these cases, the concept of a local diffusion coefficient is no longer entirely meaningful.

In the results presented here, the radial electric field is large enough to insure the maximum deviation from a flux surface, $\Delta r \sim v_d/\Omega_E$, is still very small when compared with the other physical scale lengths of the simulation. Further, particles are stopped when they reach set cutoff radii (these are usually set several Δr either side of the launch radius). Together, these largely eliminate nonlocal effects and make the calculation of a local diffusion coefficient possible.

One of the most popular methods for obtaining an estimate of the diffusion coefficient is through the mean square displacement or "dispersion" of N particles [6]

$$V(t) = \langle (x(t) - \langle x \rangle)^2 \rangle = \frac{1}{N} \sum_{i=1}^{N} (x_i(t) - \langle x \rangle)^2,$$

where

$$\langle x \rangle = \frac{1}{N} \sum_{i=1}^{N} x_i(t).$$

The estimate of D is obtained from

$$D = \frac{1}{2} \frac{dV}{dt}. \tag{27}$$

Unfortunately, the expression for D above is not valid when particles are lost to the cutoff radii during the simulation.

In order to treat the effects of particles lost at some boundary, we solve the diffusion equation

$$\frac{\partial n}{\partial t} = D \frac{\partial^2 n}{\partial x^2}$$

assuming $n(x, t) = X(x)\, T(t)$. In one dimension, $-L \leqslant x \leqslant L$ $(n(\pm L) = 0)$, the solution is

$$n = \sum_{l=0}^{\infty} A_l \exp\left(-\frac{D\pi^2(2l+1)^2\, t}{4L^2}\right) \cos\left(\frac{(2l+1)\,\pi x}{2L}\right).$$

Multiplying both sides by $\sum_{i=1}^{N} \cos(\pi x_i/2L)$, using the orthogonality property of the cosine terms, and using the fact that $x_i(t) = 0$ at $t = 0$ so that

$$N = \sum_{i=1}^{N} \cos\left(\frac{\pi x_i(0)}{2L}\right),$$

the following estimate of D is obtained

$$D = \frac{-4L^2}{\pi^2 t} \ln\left\{\frac{1}{N} \sum_{i=1}^{N} \cos\left(\frac{\pi x_i(t)}{2L}\right)\right\}. \tag{28}$$

When the x_i/L are small this reduces to the usual expression, of the form of (27).

In the present simulation, N particles are released with equal energies at $r = r_0$, but with randomized values of pitch, poloidal, and toroidal angles. Each is followed for a time $\tau_F = n\tau_{90}$ (where τ_{90} is the 90° deflection time for ions on ions and n is a positive integer) or until it reaches one of two set cutoff radii, r_c. Final values of radius, r_i and elapsed time, τ_i, are recorded for each particle. Diffusion coefficients are calculated for each ensemble using the following forms of Eq. (27)–(28).

$$D = \frac{\sum_{i=1}^{N} (r_i - \langle r \rangle)^2}{2 \sum_{i=1}^{N} \tau_i} \tag{27'}$$

$$D = \frac{-4L^2}{\pi^2 \tau_F} \ln\left\{\frac{1}{N} \sum_{i=1}^{N} \cos\left(\frac{\pi(r_i - r_0)}{2L}\right)\right\}, \tag{28'}$$

where $L = r_c - r_0$.

Equation (27′) is the limiting form of (27) as $t \to \infty$. In (28′) particles which reach r_c contribute nothing to the sum. The diffusion coefficient is evaluated from the final positions of those particles which have remained confined for $t = \tau_F$, although this form of D does allow properly for the contribution of that fraction of the distribution which is lost to the boundary, through the weighting factor $1/N$.

As long as no particles reach the cutoff radii during the simulation, (27′) is to be preferred as an estimate of D (although for most cases both forms of D will agree to at least 3 figures). When significant numbers of particles reach the cutoff radii (28′) is used to estimate D and yields accurate values as long as there is not a preferential direction in which the particle distribution moves (that is, $\langle r \rangle$ is small).

IV. Results

To obtain the results presented in this section, several (from 3–6) ensembles of 100–500 particles were run at each collision frequency. Each particle was followed

for five 90° deflection times or until it reached a cutoff radius. Typical CPU times on the CRAY-1 computers of the National Magnetic Fusion Energy Computer Center varied from 20 min for 500 particles at $\nu_{\text{eff}}/\Omega_E = 10$ to 150 min for 100 particles at $\nu_{\text{eff}}/\Omega_E = 0.01$. Charge times were 1/10 of this, however, since the numerical simulation is efficient enough to run at a priority of 0.1. A typical guiding center simulation has roughly equal CPU time at $\nu_{\text{eff}}/\Omega_E = 10$, but this time increases linearly with $(\nu_{\text{eff}}/\Omega_E)^{-1}$, since the maximum step size for numerical accuracy has been reached. From this, it is clear that the full advantages of the hybrid code are realized at very low collision frequency, where a single step in the bounce-averaged formalism can replace many hundreds of steps by guiding center equations.

Error bars are not shown for each individual data point to avoid cluttering the graphs. Typical statistical errors range from 5% at $\nu_{\text{eff}}/\Omega_E = 10$ (many runs of 500 particles) to 15–20% at $\nu_{\text{eff}}/\Omega_E = 0.01$ (fewer runs of 100 particles).

The fact that k_{FS}^2, k_{BA}^2, and k_{GC}^2 are set by the user allows for a great deal of flexibility in the hybrid formulation. For example, by setting $k_{\text{BA}}^2 = 0$ and $k_{\text{FS}}^2 = \infty$, the simulation may be run as a purely guiding center code. This was done initially with $\varepsilon_{\text{h}} = 0$ to benchmark the results with axisymmetric neoclassical predictions. Agreement was found to be very good.

As has been indicated, the simulation treats ion–ion collisions using the Lorentz collision operator, which is not momentum conserving. Conservation of momentum is important in an axisymmetric device, since accounting for the displacement of background particles due to momentum transfer by like particle collisions would exactly cancel the "diffusion" of the test particle. In a device such as a stellarator, however, this is no longer true due to the symmetry breaking in the toroidal direction. In fact, when dealing with the full collision operator, the momentum conservation part bounce-averages to zero. Thus, use of the Lorentz collision operator is appropriate to the study of ripple transport, although it should be noted that the contribution to the "axisymmetric" part of D is overestimated by its use, since the appropriate collision frequency in this case is the ion–electron.

As stated earlier, the prime motivation for the inclusion of guiding center equations was to properly handle the complicated physical processes present at the ripple trap/detrap boundary. This overcomes the major weakness of the earlier bounce-averaged simulation [12], which by its very nature did not have the necessary information to correctly describe this region of phase space and allows one to determine what effects the shortcomings of an "averaged" method entail.

In Fig. 6, D is plotted versus $\nu_{\text{eff}}/\Omega_E$ ($\nu_{\text{eff}} = \nu/2\varepsilon_{\text{h}}$) for the standard ripple profile of configuration 1 (Note: this is the configuration examined in [12] and is also Case 1 of [21]). The collision frequency was varied by changing the background density, all other quantities remaining constant. The open circles display the results obtained using the hybrid code with $k_{\text{FS}}^2 = 1.08$, $k_{\text{BA}}^2 = 0.9$, and $k_{\text{GC}}^2 = 0.75$. This choice of the k^2 boundaries was made after following a large number of collisionless orbits. No appreciable difference in diffusion rates was observed for the two signs of the electric field so that each open circle indicates essentially identical values of D for both signs of E_{r}. Solid circles are the results obtained for $E_{\text{r}} = 0$ with $k_{\text{FS}}^2 = 1.08$

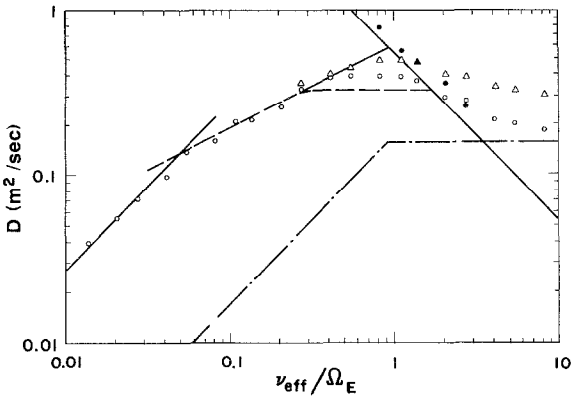

FIG. 6. D vs ν_{eff}/Ω_E for the standard ripple profile of configuration 1. Open circles are the numerical results obtained in the presence of a strong radial electric field, E_r. Solid circles denote numerical points for $E_r = 0$. Open triangles are the numerical results obtained when k_{FS}^2 is defined by (32), so as to include all toroidal effects thought to be important at low collision frequency. Solid lines represent the analytic estimates of (29) and $\frac{1}{2}$ the analytic estimate of (31). The broken (dashed) line was obtained by numerical integration of the result obtained by Galeev and Sagdeev. The dot–dash line indicates the expected magnitude and scaling of the tokamak banana and banana plateau regimes

and $k_{BA}^2 = k_{GC}^2 = 0$ (all ripple-trapped particles followed with guiding center equations). These show the $1/\nu$ scaling predicted by the estimate

$$D = \frac{4}{9\pi} (2\varepsilon_h)^{3/2} \frac{v_d^2}{\nu} \tag{29}$$

which is also plotted for reference.

At lower collision frequency the distribution function obtained by Galeev and Sagdeev using boundary layer analysis techniques has been integrated over (k^2, θ) numerically and indicated by the broken line. As the collision frequency decreases this result approaches an asymptote with slope proportional to $\sqrt{\nu}$. The magnitude of the diffusion coefficient taken from this asymptote is roughly a factor of 6 less than the usual heuristic estimate

$$D \simeq \frac{v_d^2}{(\Omega_E)^{3/2}} \nu^{1/2}. \tag{30}$$

In the region $1/\pi \lesssim \nu_{eff}/\Omega_E \lesssim 1$, the Galeev–Sagdeev result reaches saturation and becomes very flat, as described in Ref. [21]. Although this region of saturation is not as wide as was heuristically argued in [21], it is of significant extent and is the region in which D obtains its largest values at low collision frequency.

At the lowest collision frequencies, the diffusion coefficient shows the linear scaling with ν predicted by various authors [2–4]. The numerical coefficient of the line drawn in this region on Fig. 6 is not predicted by any theory, but is instead, a "best

fit" to the data. It is approximately half as large as the result predicted by Mynick [4],

$$D \simeq \left(\frac{v_d}{\Omega_E}\right)^2 \frac{\varepsilon_h}{\varepsilon_t(2\varepsilon_h)^{1/2}}\nu. \tag{31}$$

In this paper we are primarily interested in transport processes arising from particles trapping and detrapping in the helical well. However, if we redefine k_{FS}^2 as

$$k_{FS}^2 = \frac{\kappa/\mu B_0 - 1 + \varepsilon_t + \varepsilon_h}{2(\varepsilon_t + \varepsilon_h)} \tag{32}$$

then all particles with $k_{FS}^2 > 1$ are definitely "passing" particles, being neither helically nor toroidally trapped since (32) has been constructed to measure depth in the "total" (toroidal and helical) ripple. When the hybrid simulation is run with this definition of k_{FS}^2, ripple-trapped particles are followed through the conservation of J, particles near the helical trapping boundary as well as *all* toroidally blocked particles are followed with guiding center equations and passing particles are allowed to stream along field lines. This allows for all toroidal diffusion mechanisms expected to be important at low ν. Results obtained from the hybrid code with k_{FS}^2 as defined in (32) are shown in Fig. 6 as open triangles. Again, there was no variation in D with the sign of E_r. As expected, toroidal banana effects add significantly to the diffusion coefficient at the higher collision frequencies and nearly vanish once the unsaturated Galeev–Sagdeev regime is reached. The expected magnitude and scaling of the axisymmetric banana and banana plateau regimes are shown in Fig. 6 by a dot–dash line.

In Fig. 7, D is plotted versus ν_{eff}/Ω_E for the ripple profile of (3). To obtain ν_{eff} we have averaged (3) over one poloidal transit. For configuration 1, the "averaged"

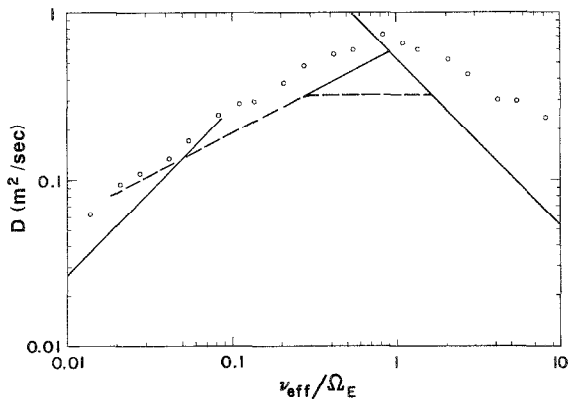

FIG. 7. D vs ν_{eff}/Ω_E for the θ dependent ripple profile of configuration 1. Open circles are the results obtained in the presence of a strong radial electric field. The line of Fig. 6 pertaining to ripple diffusion are reproduced for comparison.

value of ε_h obtained in this manner differs by less than 5% from its traditional value. The lines of Fig. 6 are reproduced for reference.

Although the magnitudes of the averaged values of ε_h may be nearly equal for the two ripple profiles, it is clear that the addition of poloidal dependence, even though rather weak, has a significant effect on the diffusion coefficient. The saturation of the Galeev–Sagdeev regime is much slower than that obtained in Fig. 6 for the standard ripple profile. Further, the Galeev–Sagdeev result would seem to persist at much lower collision frequencies, finally meeting the ν regime at the lowest collision frequencies investigated. No analytic theory exists which treats the ripple profile of (3), however, an examination of the usual analytic treatment is capable of providing an heuristic explanation of the observed behavior.

In analytic theory, one finds the particle flux through a given surface by multiplying dr/dt by the perturbed portion of the distribution function, f^1, and then integrating over the appropriate volume element. An analytic expression for the diffusion coefficient is obtained from this process. In the standard picture in which $\varepsilon_h = \varepsilon_h(r)$, the average of (22) over one bounce yields $\langle dr/dt \rangle \approx v_d \sin\theta$. The perturbed portion of the distribution function is made up of terms that vary as $\sin\theta$, $f^1_{\sin\theta}$, and $\cos\theta$, $f^1_{\cos\theta}$. Given the form of $\langle dt/dt \rangle$ above, the $\cos\theta$ term contributes nothing to the particle flux integral. Thus, one is interested only in the variation of $f^1_{\sin\theta}$ with collision frequency since it is this variation which gives rise to different transport rates and scalings.

In the range of collision frequencies for which $\nu_{\text{eff}} \lesssim \Omega_E$, Galeev and Sagdeev [3] obtained a result for which $f^1_{\sin\theta}$ was highly localized just below the $k^2 = 1$ boundary. This "boundary layer," of width $\Delta k^2 \sim (\nu_{\text{eff}}/\Omega_E)^{1/2}$, gives rise to the $\sqrt{\nu}$ scaling expected in this regime. As the collision frequency becomes larger, this highly localized distribution broadens until it extends throughout the entire ripple-trapped region [21]. At this point the number of particles participating in the diffusion process saturates, although the mean value of k^2 indicated by $f^1_{\sin\theta}$ continues to move toward $k^2 = 0$. Since $\langle dr/dt \rangle$ is constant with respect to k^2, this movement has no effect on the particle flux integral and the diffusion coefficient is independent of collision frequency in this region.

Finally, at still higher collision frequencies, the Galeev–Sagdeev result is no longer valid as the collision frequency is large enough that the electric field has little opportunity to affect a particle's motion. The transport coefficients are expected to scale as ν^{-1} and $f^1_{\sin\theta}$ is expected to be stationary in k^2 with a dependence given by $(1-k^2)$.

However, this development is altered when θ dependent ripple profiles such as that of (3) are considered. In this case, averaging (22) and substituting for $\partial\varepsilon_h/\partial\theta_0$ yields

$$\left\langle \frac{dr}{dt} \right\rangle \approx v_d \sin\theta \left\{ 1 + \frac{\varepsilon_h z_0 \rho}{\varepsilon_t (z_0^2 + \rho^2 - 2 z_0 \rho \cos\theta)} \langle \cos(l\theta + p\phi) \rangle \right\}, \tag{33}$$

where $\langle \cos(l\theta + p\phi) \rangle$ is given by (19). An examination of $\langle \cos(l\theta + p\phi) \rangle$ shows

that it varies from $+1$ to -1, being positive over the great majority of k^2 values. In particular, it is positive for $0 \leqslant k^2 \lesssim 0.83$ and negative for $0.83 \lesssim k^2 < 1$.

When $f^1_{\sin\theta}$ is highly peaked just below $k^2 = 1$, $\langle dr/dt \rangle$ is less than $v_d \sin\theta$ for the majority of particles. However, as the collision frequency increases and $f^1_{\sin\theta}$ spreads out, $\langle dr/dt \rangle$ becomes larger than $v_d \sin\theta$ for more and more of the ripple-trapped population. When $f^1_{\sin\theta}$ extends throughout the ripple-trapped region the number of particles involved in the diffusion process will still, in all likelihood, saturate. However, $\langle dr/dt \rangle$ is now dependent on k^2 and will continue to increase, on average, as the mean value of k^2 indicated by $f^1_{\sin\theta}$ continues to move toward $k^2 = 0$. Thus even though the fraction of the distribution contributing to the diffusion is roughly constant, D can still increase with ν, as a result of the variation of $\langle dr/dt \rangle$ with k^2.

In the ν^{-1} regime, since $f^1_{\sin\theta}$ is largely stationary and characterized by small values of k^2, the "average" radial step is increased according to (33), and hence the magnitude of the diffusion coefficient is increased. However, the ν^{-1} scaling should be unaffected. The development in this regime is very similar to that presented by Mynick *et al.* [17], for a $\sigma = -1$ configuration (helical ripple largest at the outside of the device), although the effect is not as pronounced for a ripple profile of the form of (3).

Expressed in terms of k^2, the Galeev–Sagdeev boundary layer width is approximately $(\nu_{\text{eff}}/\Omega_E)^{1/2}$. Given this and the previous heuristic argument, one might expect the diffusion coefficients obtained for the traditional and θ-dependent ripples to be roughly equal at $\nu_{\text{eff}}/\Omega_E = 0.05$. Through the higher collision frequencies of the Galeev–Sagdeev regime the diffusion coefficient for the θ dependent ripple should steadily increase relative to the traditional results plotted in Fig. 6. As the ν^{-1} regime is entered this increase should cease and the diffusion coefficient should assume the same scaling for the θ-dependent ripple as for the traditional ripple, albeit at a higher value.

This heuristic argument is relatively well supported by the results in Fig. 7. One might also argue that the results would be explained just as well by claiming that it is the deepest wells which contribute most substantially to the transport, and therefore the maximum value of ε_h, or a value of ε_h approaching the maximum, is the appropriate one to use in estimating the diffusion coefficient. This argument is attractive in that it explains the movement of the ν regime to lower collision frequencies. However, it would not explain the reduction of the saturated Galeev–Sagdeev regime. It may be possible that both explanations are valid to a greater or lesser degree at various collisionalities.

In Fig. 8, D is plotted versus $\nu_{\text{eff}}/\Omega_E$ for configuration 2, $\varepsilon_h = \varepsilon_h(r)$. This configuration was also examined with the bounce-averaged code in [21]. No dependence of D on the sign of the radial electric field was observed in that work. Because of this, we have chosen to examine only the case $E_r < 0$ in the present paper. For the parameters of configuration 2 it is not entirely clear what value of ε_h should be used in plotting $\nu_{\text{eff}}/\Omega_E$ since toroidal effects substantially reduce the actual depth of the well over much of the poloidal cross section. We have chosen to

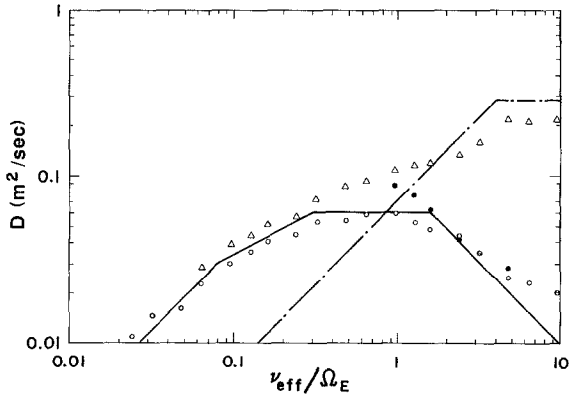

FIG. 8. D vs ν_{eff}/Ω_E for the standard ripple profile of configuration 2. The symbols are as in Fig. 6. The solid line was obtained by scaling the results of Fig. 6 which pertain to ripple diffusion processes. The dot–dash line indicates the expected magnitude and scaling of the tokamak banana and banana plateau regimes.

use its maximum value in calculating the abscissa of Fig. 8, since this choice correctly places each regime in its expected range of validity (i.e., saturated Galeev–Sagdeev regime in the range $1/\pi \lesssim \nu_{eff}/\Omega_E \lesssim 1$, ν^{-1} regime beginning at $\nu_{eff}/\Omega_E \gtrsim 1$, etc.). Because of the very small ripples which exist in a large portion of phase space and which contribute only minimally to transport, the fraction of particles taking part in the major diffusion process will be less than the usual heuristic estimate, $f \approx \sqrt{2\varepsilon_h}$, and consequently, transport rates will fall. This is borne out by the numerical results.

It is interesting to note that an estimate of the position of the transition from ν to $\sqrt{\nu}$ regimes which uses (31) predicts the complete lack of a $\sqrt{\nu}$ regime for this configuration in which $\varepsilon_h \ll \varepsilon_t$. Instead, there is a very considerable $\sqrt{\nu}$ regime, reduced only slightly in extent from that obtained in Fig. 6. The factor of $\varepsilon_h/\varepsilon_t$ in (31) was obtained by assuming that the time a typical particle spent ripple trapped was much greater than the time it spent toroidally trapped. For this configuration, the opposite limit is appropriate and (31) must have the factor $\varepsilon_h/\varepsilon_t$ removed to reflect this.

The solid lines on Fig. 8 were obtained by scaling the results of Fig. 6 to the parameters of configuration 2. Since v_d and Ω_E do not change between the two cases, this involved only a substitution for ε_h, where appropriate, and multiplying all results by $\frac{1}{3}$, which is a crude estimate as to the amount of phase space in which ripples of significant depth exist. The factor of $\varepsilon_h/\varepsilon_t$ was also removed in the ν regime. The expected scaling of D due to axisymmetric bananas is shown by the dot–dash line.

Finally, in Fig. 9, D is plotted versus ν_{eff}/Ω_E for the θ-dependent ripple profile of configuration 2. As was shown in Fig. 2, the standard and θ-dependent ripple profiles differ so dramatically for this configuration that comparision of the two is probably not a meaningful exercise. Averaging (3) over a poloidal transit, we

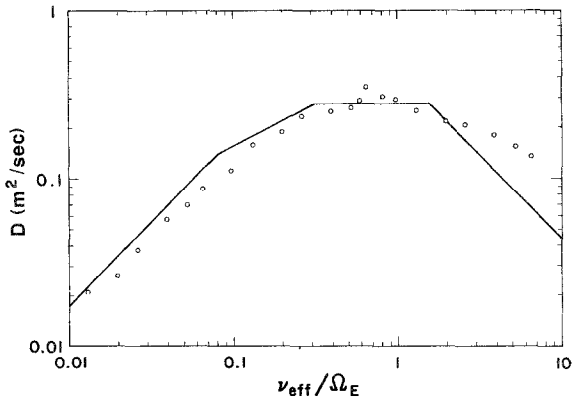

FIG. 9. D vs $\nu_{\text{eff}}/\Omega_E$ for the θ-dependent ripple profile of configuration 2. The symbols are as in Fig. 7. The solid line was obtained by scaling the results of Fig. 6 which pertain to ripple diffusion processes. An "averaged" value of ε_h was used to make this possible.

obtain an averaged value of ε_h which is greater than its traditional counterpart by a factor of $\frac{7}{3}$. Again, to produce the lines of Fig. 9, we have scaled the results of Fig. 6, using this new value of ε_h. No additional numerical factor was used, however, as wells of significant depth exist over the entire poloidal cross section. The strange peaked behavior of the diffusion coefficient around $\nu_{\text{eff}}/\Omega_E = 0.5$ is an as yet unexplainable quirk in the data. However, this peak is completely reproduceable and has been found to exist when this range of collision frequencies is examined using guiding center equations exclusively.

V. CONCLUSION

An efficient and accurate computer program has been developed to examine particle orbits and the accompanying transport at low collision frequency in a stellarator field. It has been shown that allowing for the local toroidal variation of this magnetic field within a single ripple period produces a much more complex range of trapping-detrapping behavior than allowed for in analytic theory. Accurate expressions which reflect this toroidal variation have been constructed for k^2, which indicates trapping state, and for J, the longitudinal adiabatic invariant. These forms of J and k^2 have been incorporated into a "hybrid" bounce-averaged/guiding center computer simulation. The simulation rapidly describes the trajectories of ripple-trapped particles while correctly treating the important physical effects at the ripple-trap/detrap boundary, allowing the most accurate description to date of ripple transport at low collision frequency.

Two very different stellarator configurations have been examined, one a medium aspect ratio device for which the magnitude of the helical ripple, ε_h, is slightly greater than that of the toroidal ripple, ε_t, and the second a low aspect ratio stellarator for which $\varepsilon_t \gg \varepsilon_h$. The magnitude of the diffusion coefficient, D, is less for

these devices than found earlier [21] although its scaling is generally similar. The principal difference arises in the range of collision frequencies where D is expected to scale as $\nu^{1/2}$. In the earlier work which employed a purely bounce-averaged formulation to follow ripple-trapped particles it was unclear whether the $\nu^{1/2}$ scaling was evident, while in the current work this region is well defined. The flat transition region between the regimes which scale as $\nu^{1/2}$ and ν^{-1} found in Ref. [21] is confirmed using the hybrid formulation.

These results for the usual analytic model of the helical ripple, $\varepsilon_h = \varepsilon_h(r)$, have been contrasted with those obtained for a more realistic model in which $\varepsilon_h = \varepsilon_h(r, \theta)$. The more realistic ripple profile has been shown to alter both the magnitude and scaling of the diffusion coefficient with collision frequency, even when the poloidal dependence of ε_h is weak. The diffusion coefficient is increased at all collision frequencies examined and the extent of the flat transition region is reduced. This effect is due to the additional term introduced into the radial drift velicity, which unlike the usual $v_d \sin\theta$ term is dependent on a particle's depth in the helical well.

REFERENCES

1. A. A. GALEEV, R. Z. SAGDEEV, H. P. FURTH, AND M. N. ROSENBLUTH, *Phys. Rev. Lett.* **22**, 511 (1969).
2. A. A. GALEEV, AND R. Z. SAGDEEV, *Sov. Phys. Usp.* **12**, 810 (1970).
3. A. A. GALEEV, AND R. Z. SAGDEEV, *Reviews of Plasma Physics*, Vol. 7 (Consultants Bureau, New York, 1975).
4. H. E. MYNICK, *Phys. Fluids* **26**, 2609 (1983).
5. L. M. KOVRIZHNYKH, *Nucl. Fusion* **24**, 851 (1984).
6. A. H. BOOZER, AND G. KUO-PETRAVIC, *Phys. Fluids* **24**, 851 (1981).
7. R. E. POTOK, P. A. POLITZER, AND L. M. LIDSKY, *Phys. Rev. Lett.* **45**, 1328 (1980).
8. H. WOBIG, *Z. Naturforsch a* **37**, 906 (1982).
9. M. WAKATANI, *Nucl. Fusion* **23**, 817 (1983).
10. W. DOMMASCHK, W. LOTZ, AND J. NUHRENBERG, *Nucl. Fusion* **24**, 794 (1984).
11. R. H. FOWLER, J. A. ROME, AND J. F. LYON, *Phys. Fluids* **28**, 338 (1985).
12. W. N. G. HITCHON, C. D. BEIDLER, H. E. MYNICK, AND J. L. SHOHET, *Nucl. Fusion* **25**, 105 (1985).
13. J. S. TOLLIVER, Ph.D. thesis, University of Tennessee, Knoxville, 1984 (unpublished).
14. H. E. MYNICK, AND W. N. G. HITCHON, *Nucl. Fusion* **26**, 425 (1986).
15. W. N. G. HITCHON, K. D. MCLENITHAN, AND H. E. MYNICK, *Nucl. Fusion* **23**, 1143 (1983).
16. T. E. STRINGER, *Nucl. Fusion* **12**, 689 (1972).
17. H. E. MYNICK, T. K. CHU, AND A. H. BOOZER, *Phys. Rev. Lett.* **48**, 322 (1982).
18. K. C. SHAING AND S. A. HOKIN, *Phys. Fluids* **26**, 2136 (1983).
19. V. E. BYKOV, A. V. GEORGIEVSKIJ, V. G. PELETMINSKAYA, A. V. KHODYACHIKH, AND A. A. SHISHKIN, *Nucl. Fusion* **24**, 1195 (1984).
20. A. H. BOOZER, *Phys. Fluids* **23**, 904 (1980).
21. W. N. G. HITCHON, C. D. BEIDLER, H. E. MYNICK, AND J L. SHOHET, *J. Plasma Phys.* **34**, 327 (1985).